

Metal-organic framework membranes with single-atomic centers for photocatalytic CO₂ and O₂ reduction

Yu-Chen Hao¹, Li-Wei Chen¹, Jiani Li¹, Yu Guo², Xin Su¹, Miao Shu³, Qinghua Zhang⁴, Wen-Yan Gao¹, Siwu Li¹, Zi-Long Yu¹, Lin Gu⁴, Xiao Feng¹, An-Xiang Yin¹, Rui Si³, Ya-Wen Zhang², Bo Wang^{1,5} & Chun-Hua Yan²

The demand for sustainable energy has motivated the development of artificial photosynthesis. Yet the catalyst and reaction interface designs for directly fixing permanent gases (e.g. CO₂, O₂, N₂) into liquid fuels are still challenged by slow mass transfer and sluggish catalytic kinetics at the gas-liquid-solid boundary. Here, we report that gas-permeable metal-organic framework (MOF) membranes can modify the electronic structures and catalytic properties of metal single-atoms (SAs) to promote the diffusion, activation, and reduction of gas molecules (e.g. CO₂, O₂) and produce liquid fuels under visible light and mild conditions. With Ir SAs as active centers, the defect-engineered MOF (e.g. activated NH₂-UiO-66) particles can reduce CO₂ to HCOOH with an apparent quantum efficiency (AQE) of 2.51% at 420 nm on the gas-liquid-solid reaction interface. With promoted gas diffusion at the porous gas-solid interfaces, the gas-permeable SA/MOF membranes can directly convert humid CO₂ gas into HCOOH with a near-unity selectivity and a significantly increased AQE of 15.76% at 420 nm. A similar strategy can be applied to the photocatalytic O₂-to-H₂O₂ conversions, suggesting the wide applicability of our catalyst and reaction interface designs.

¹Ministry of Education Key Laboratory of Cluster Science, Beijing Key Laboratory of Photoelectronic/Electrophotonic Conversion Materials, School of Chemistry and Chemical Engineering, Beijing Institute of Technology, Beijing, P. R. China. ²Beijing National Laboratory for Molecular Sciences, State Key Laboratory of Rare Earth Materials Chemistry and Applications, PKU-HKU Joint Laboratory in Rare Earth Materials and Bioinorganic Chemistry, College of Chemistry and Molecular Engineering, Peking University, Beijing, P. R. China. ³Shanghai Synchrotron Radiation Facility, Shanghai Institute of Applied Physics, Chinese Academy of Sciences, Shanghai, P. R. China. ⁴Institute of Physics, Chinese Academy of Sciences, Beijing, P. R. China. ⁵Advanced Technology Research Institute (Jinan), Beijing Institute of Technology, Jinan, P. R. China. ✉email: yin@bit.edu.cn; sirui@sinap.ac.cn; bowang@bit.edu.cn

In nature, solar energy is harnessed by photosynthesis and stored in fossil fuels through slow geochemical fossilization processes. Resembling the functionalities of green leaves, interdisciplinary researchers have developed various photosynthetic systems across the natural–artificial spectrum^{1–8}. Although a solar-to-electric energy conversion rate of over 20% can be achieved by inorganic photovoltaic devices⁹, abiotic photosynthetic systems that can fix naturally abundant permanent gases (e.g., CO₂, O₂) into value-added liquid fuels still face challenges in productivity and selectivity^{6,10}.

First, challenged by the large kinetic barriers, both homogeneous and heterogeneous photocatalysts feature inherent advantages and trade-offs for such applications¹¹. On one hand, homogeneous catalysts possess highly dispersed and accessible active sites with accurately tailored structures for specific reactions but poor product isolation and/or long-term stability^{12,13}. On the other hand, conventional heterogeneous approaches exhibit enhanced product separation, but suffer from smaller active surface areas and limited accessibility to the active sites¹¹. One promising strategy bridging homogeneous and heterogeneous photocatalysis is to develop catalysts with atomically dispersed active centers^{14–17}, which can significantly improve the accessibility and utilization of catalytic sites while facilitate the separation of products. For instance, photocatalysts with atomically dispersed active centers can effectively reduce CO₂ to CO^{15–17}, suggesting the advantages of such single-atom photocatalysts (SAPCs); while systematic studies are still in great need to reveal the mechanism for reducing CO₂ on single-atomic sites to produce a much wider range of value-added products (e.g., hydrocarbons, alcohols, and carboxylates, etc.) with higher selectivity and efficiency.

Second, the efficiency for reducing such permanent gas is further limited by the gas–liquid–solid reaction interface. The traditional photocatalytic interface design with dissolving or submerging catalysts in aqueous solutions is optimal for reactions involving only liquid reactants (e.g., water splitting)⁴. The limited solubility and sluggish diffusion kinetics of permanent gas in aqueous solutions strongly retard the following catalytic conversion on the heterogeneous reaction interface^{18,19}. In addition, the overwhelming competitions from water adsorption on the flooded catalyst surface further suppress the reduction of gas molecules with the undesired hydrogen evolution reaction (HER)^{6,19,20}. Consequently, photoreduction of insoluble and stable gas molecules on the three-phase catalysis interface inevitably confronts three formidable challenges: (i) the kinetically hindered diffusion, (ii) the sluggish surface adsorption, and (iii) the inefficient activation and catalytic conversion of the gas reactants. Fabricating films of stacked nanoparticles, including solid semiconductors^{21–23} and porous metal-organic frameworks (MOFs)^{24,25}, and catalyzing photocatalytic gas reduction on the gas–solid interfaces with water vapor as proton sources could partially solve the mass transfer limitation by avoiding the water flooding of the catalyst surface. However, such systems still suffer from slow mass transfer with the only driving force from spontaneous thermal motions of gaseous molecules. Therefore, to further promote the photoreduction of permanent gas to storable and portable chemical fuels, advanced photocatalytic systems should consist of both highly dispersed active sites lowering the reaction energy barriers and high-throughput reaction interfaces, with large surface areas boosting the diffusion of gaseous reactants to the active sites.

MOFs, an emerging class of porous crystalline materials with large surface areas, high porosity, and tunable functionalities, prove to be a promising candidate for heterogeneous photocatalytic reductions^{26–29}, showing great potential for solving the aforementioned challenges in both reaction kinetics and mass

transfer process. Here, combining the advantages of porous MOF substrates and single-atom (SA) catalytic centers, we introduce gas-permeable membranes consisting of structurally tailored SA/MOFs particles for high-efficiency and high-throughput photocatalytic gas reduction reactions (Fig. 1a, b). Single-atom iridium (Ir₁) and palladium (Pd₁) are anchored on the MOF nodes to serve as the catalytic hydrogenation centers for CO₂ and O₂, respectively (Fig. 1b). The defect-engineering of MOF matrix can not only enhance their light harvesting capability but also tailor the chemical structures of their oxide nodes (e.g., the Zr–O nodes of NH₂-UiO-66) to finely control their interactions to the introduced metal single atoms (SAs). The activated NH₂-UiO-66 (denoted as A-aUiO hereafter) substrate can tailor the electronic structures of the supported metal species to enhance their catalytic reactivity. For instance, with stronger metal-supporter interactions (SMSI), Ir₁/A-aUiO exhibited a near-unity HCOOH evolution selectivity in photocatalytic CO₂ reduction, while Ir nanoparticles supported by A-aUiO (IrNPs/A-aUiO) showed a much lower HCOOH selectivity of 16.5%. Moreover, the high porosity of SA/MOF membranes allows the creation of gas-membrane-gas (GMG) configuration, which boosts the high-throughput diffusion of humid CO₂ to the metal SAs located at the vast gas–solid reaction interfaces within the interconnected MOF pores. Compared with the traditional gas–liquid–solid reaction interface, such high-throughput gas–solid interface design can significantly increase the availability of gaseous reactants in the vicinity of each catalytic centers (e.g., SAs). Consequently, bridging advanced catalytic center and reaction interface designs, our Ir₁/A-aUiO membranes can catalyze the CO₂-to-HCOOH photoreduction with near-unity selectivity and a HCOOH activity of 3.38 mmol g_{cat}⁻¹ h⁻¹ (the term “cat” refers to the hybrid metal species and supporters, such as metal/MOFs and metal/oxides, hereafter), exceeding 6.5 and 338 times that of the Ir₁/A-aUiO particles and the IrNPs/A-aUiO particles, respectively. Moreover, following similar optimization strategy, the Pd₁/A-aUiO membranes can convert humid O₂ to H₂O₂ with an activity of 10.4 mmol g_{cat}⁻¹ h⁻¹ under visible light, which is more than 73-fold higher than that showed by the PdNPs/A-aUiO (0.14 mmol g_{cat}⁻¹ h⁻¹) powders, verifying the wide applicability of our catalyst and reaction interface designs.

Results and discussion

Catalyst synthesis. We screened a series of photosensitizers, including MOFs, inorganic semiconductors, and coordination complex, as the hosts of metal SA active centers and the building blocks of our photocatalysis membranes. Among these candidates, NH₂-UiO-66 (aUiO), a kind of representative MOF materials³⁰, represented a promising candidate with unique advantages such as high photoactivity, porosity, specific surface area, and water stability^{30,31}. Especially, the versatile chemical tunability of such MOF materials allowed us to modify their chemical structures, and light harvesting capabilities at the molecular level for anchoring and sensitizing external metal species with rationally designed catalytic properties^{32,33}. Typically, monodispersed aUiO particles were prepared by solution method with the ligands (2-aminoterephthalic acid) partially replaced by acetates (Supplementary Fig. 1). These acetates were removed afterwards by activating the as-obtained aUiO particles under elevated temperature in a vacuum oven to obtain A-aUiO with missing linkers, and abundant defects on the edges of the Zr₆O₄(OH)₄(-CO₂)_{12-x} octahedral secondary building units (SBUs, where *x* represents number of missing linkers per SBU)³⁴ (Supplementary Fig. 2). Compared with the pristine aUiO particles, such defects provided abundant anchoring sites to bond the subsequently introduced metal (e.g., Ir and Pd) species to

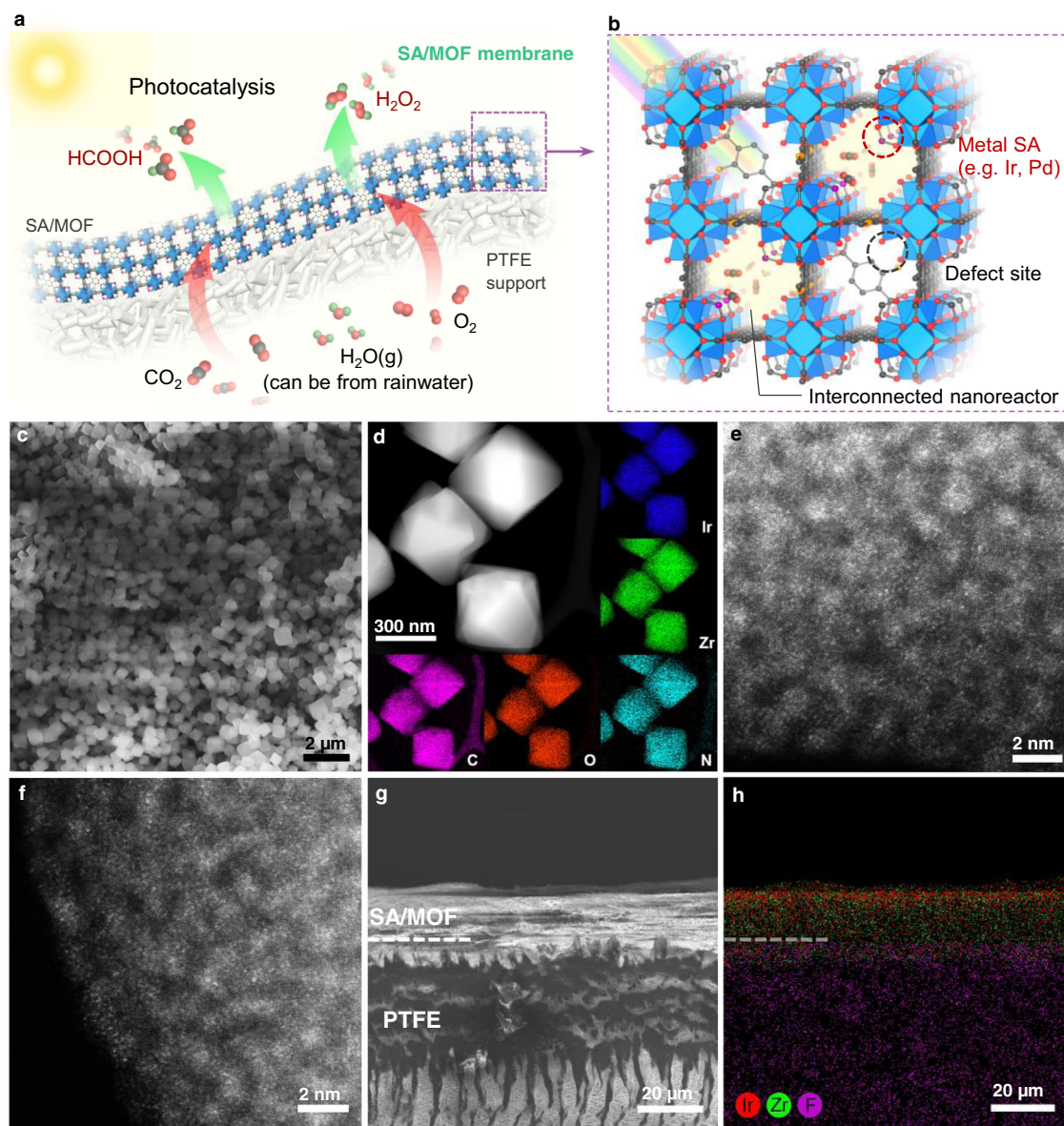


Fig. 1 Schematic illustration and structural characterization of the SA/MOF membranes. **a** Humidified gases (e.g., CO_2 , O_2) can be fed through the gas-permeable MOF/PTFE membranes and photocatalytically reduced to value-added chemicals (e.g., HCOOH and H_2O_2) under visible light irradiation and ambient conditions. **b** With controllable defect-engineering, specific metal SAs (e.g., Ir and Pd) can be precisely anchored on the edges of the $\text{Zr}_6\text{O}_4(\text{OH})_4(-\text{CO}_2)_{12-x}$ octahedral to act as programmable catalytic centers for catalyzing different reactions, such as photocatalytic CO_2 -to- HCOOH and O_2 -to- H_2O_2 conversion. The open and interconnected MOF pores serve as the nanoreactors facilitating the diffusion and conversion of gas reactants. **c** SEM image for $\text{Ir}_1/\text{A-aUiO}$ particles. **d** HAADF-STEM image and corresponding EDS maps for $\text{Ir}_1/\text{A-aUiO}$ particles. **e**, **f** AC-HAADF-STEM images for **e** $\text{Ir}_1/\text{A-aUiO}$ and **f** $\text{Pd}_1/\text{A-aUiO}$, indicating the atomic dispersion of metal species in A-aUiO matrixes. **g**, **h** SEM image (**g**) and corresponding EDS mapping (**h**) for the cross section of $\text{Ir}_1/\text{A-aUiO}/\text{PTFE}$ membranes.

obtain our SA/MOF particles and membranes (Supplementary Figs. 3–11).

Selected metal single-atoms (SAs) (e.g., Ir and Pd) were then incorporated into the A-aUiO particles by impregnation and annealing treatments (see “Methods” section). For instance, Ir SAs (1.4 wt%) could be highly dispersed in A-aUiO matrix to form $\text{Ir}_1/\text{A-aUiO}$ particles, as revealed together by the scanning electron microscopy (SEM) image, high-angle annular dark-field scanning TEM (HAADF-STEM) image, and corresponding energy-dispersive X-ray spectroscopy (EDS) maps, as well as aberration-corrected HAADF-STEM (AC-HAADF-STEM)

images (Fig. 1c–e and Supplementary Fig. 4). Extended X-ray absorption fine structure (EXAFS) analysis exhibited the existence of Ir–O bonds with the average coordination number of 3.8 and the absence of Ir–Ir bonding (Supplementary Fig. 5 and Table 1), further verifying the single-atomic dispersion of Ir species in the $\text{Ir}_1/\text{A-aUiO}$ particles. Lowering the Ir loading to 0.7 wt% resulted in sparser dispersion of Ir SAs in $\text{Ir}_1/\text{A-aUiO}$ (Supplementary Figs. 6 and 7), while increasing the loading of Ir to 2.7 wt.% and annealing the hybrids under reducing atmosphere (H_2/Ar , 1/4 v/v) led to the formation of A-aUiO containing both Ir SAs and small clusters ($\text{Ir}_x/\text{A-aUiO}$, Supplementary Figs. 8 and 9). Similarly, Pd

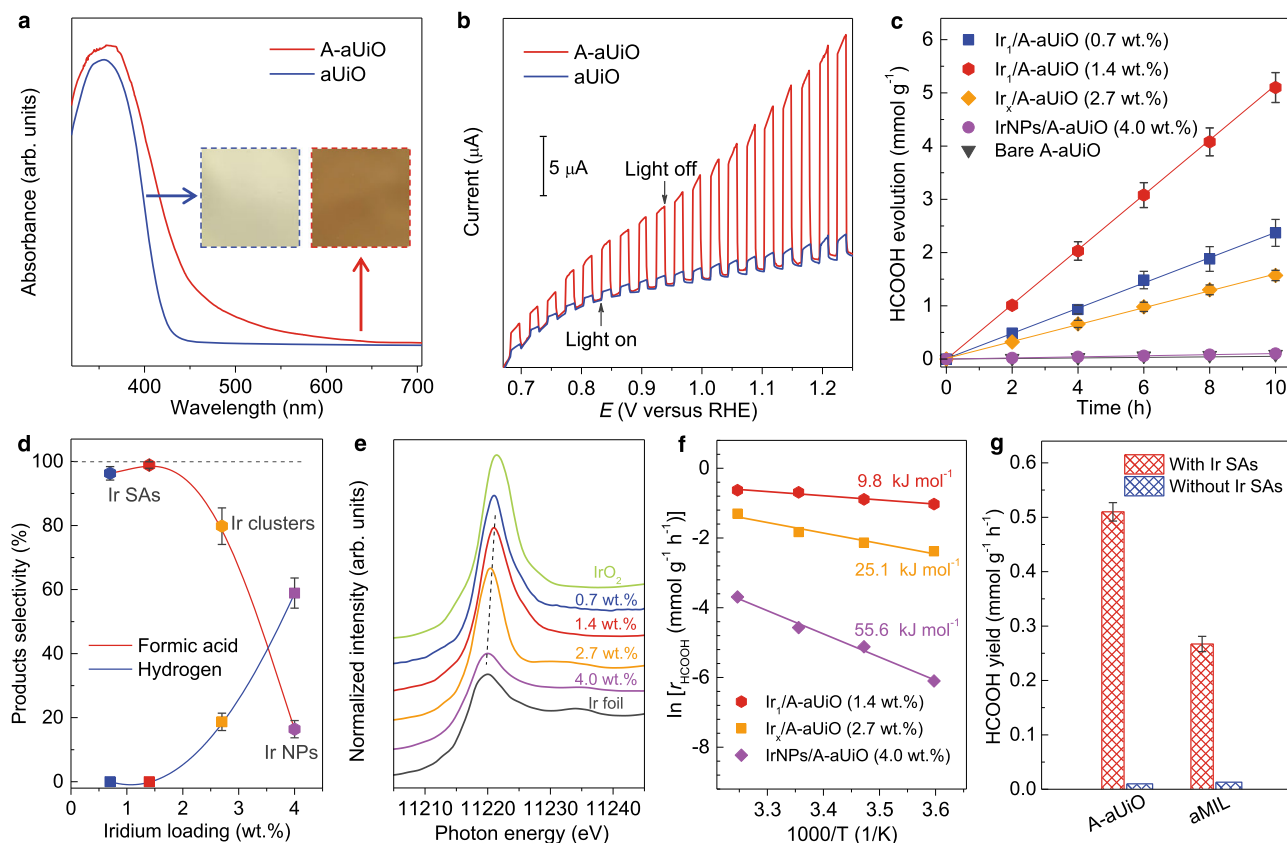


Fig. 2 Photocatalytic CO₂RR on SA/MOF powder catalysts. **a, b** The enhancing of light harvesting and conversion efficiency for A-aUiO through defects engineering. UV-Vis diffusive reflectance spectra (**a**) and photocurrent-potential curves (**b**) for A-aUiO and aUiO samples, respectively. Inset in **a**: Digital photograph showing the color of aUiO and A-aUiO samples. **c** Time course of HCOOH evolution on A-aUiO, Ir₁/A-aUiO, Ir_x/A-aUiO and IrNPs/A-aUiO catalysts. **d** HCOOH and H₂ selectivity as a function of Ir loadings in Ir₁/A-aUiO catalysts. **e** Ir L-edge XANES spectra of Ir₁/A-aUiO catalysts with different Ir loadings. Ir foil and IrO₂ were used as standards. The first maximum of the XANES curves after the absorption edge (dashed line) shows gradual positive movement with decreasing Ir loading, suggesting the metallicity of the Ir species was gradual decreased. **f** Apparent activation energy (E_{app}) of various catalysts for HCOOH generation. **g** HCOOH yields on A-aUiO and aMIL catalysts with and without Ir SAs modification. All the photocatalytic reactions were performed under visible light (>420 nm) irradiation and using isopropanol (20 v/v% in water) as sacrificial agents. Error bars were calculated by carrying out three parallel catalysis reactions.

(0.8 wt%) could also be atomically dispersed in A-aUiO to form Pd₁/A-aUiO, as confirmed by AC-HAADF-STEM and EXAFS results (Fig. 1f and Supplementary Figs. 10 and 11).

These SA/A-aUiO particles were then deposited onto commercially available porous polytetrafluoroethylene (PTFE) films in a layer-by-layer manner to fabricate flexible and gas-permeable membranes through facile filtration protocols (Fig. 1g, h and Supplementary Figs. 12–16). The hierarchical channels of the PTFE films (Fig. 1g) and the interconnected pores of the SA/A-aUiO particles naturally resembled the stomata of green leaves, facilitating the direct diffusion of gas molecules and the collision of them onto the open metal SA catalytic centers within the pores and channels of MOFs.

Photocatalytic CO₂ reduction reaction (CO₂RR). We then performed photocatalytic CO₂RR at the traditional three-phase (with Ir₁/A-aUiO particles) and our re-designed reaction interfaces (with Ir₁/A-aUiO membranes), to demonstrate the advantages of single-atomic catalytic centers and high-throughput gas–solid reaction interfaces. Water and isopropanol were used as the proton sources and sacrificial agents, respectively. A 300 W Xe lamp equipped with a 420 nm long-pass filter was used as the visible light source. As revealed by ultraviolet-visible absorption

spectra (Fig. 2a), creating missing linkers and coordination defects on the Zr–O nodes dramatically enhanced the visible light absorption efficiency of aUiO particles (Supplementary Fig. 17)³⁵, shifting their absorption band edge up to 600 nm in the visible region. Compared with the pristine defect-deficient aUiO and other typical semiconductor photocatalytic hosts, such as titanium dioxide (TiO₂) and carbon nitride (C₃N₄), A-aUiO exhibited much higher photon-to-electron conversion efficiency under visible light (>420 nm) irradiation (Fig. 2b and Supplementary Figs. 18 and 19). The photogenerated electrons could be then effectively captured by active centers such as metal SAs and nanoparticles (NPs) (Supplementary Fig. 20).

To investigate the intrinsic activity and catalytic mechanism of our catalysts, we first monitored the CO₂RR on powder photocatalysts in the conventional particle-in-solution (PiS) mode with gas–liquid–solid reaction interfaces (Supplementary Fig. 21). As shown in Fig. 2c, bare A-aUiO showed no observable CO₂RR activity. The IrNPs/A-aUiO catalysts (with an optimized metal loading content of 4.0 wt%, Supplementary Figs. 22 and 23) exhibited a HCOOH generation activity of 10 μmol_{g_{cat}}⁻¹ h⁻¹ (i.e., 10 μmol of HCOOH per gram of metal/A-aUiO catalysts per hour) with a poor selectivity of only 16.5% (Fig. 2c and Supplementary Fig. 24). The Ir_x/A-aUiO samples, containing

both Ir clusters and SAs, showed higher HCOOH evolution activity ($0.16 \text{ mmol g}_{\text{cat}}^{-1} \text{ h}^{-1}$) and selectivity (79.8%) (Fig. 2c, d). In sharp contrast, the 0.7 wt% Ir₁/A-aUiO catalysts exhibited a HCOOH generation rate of $0.24 \text{ mmol g}_{\text{cat}}^{-1} \text{ h}^{-1}$ with a high selectivity of 96.3%. Increasing the Ir SAs loading to 1.4 wt% elevate the HCOOH activity to as high as $0.51 \text{ mmol g}_{\text{cat}}^{-1} \text{ h}^{-1}$ with a near-unity selectivity (Supplementary Figs. 24–26). The significant differences in CO₂RR reactivity among iridium SAs, clusters, and NPs (all supported by A-aUiO) suggested that the chemical structures of Ir species and their interactions with the A-aUiO hosts played a critical role in the selective photoreduction of CO₂ to HCOOH. Compared with Ir clusters and nanoparticles, the Ir SAs were more positively charged (+3 to +4) as revealed by X-ray absorption near-edge structure (XANES) and X-ray photoelectron spectroscopy (XPS) analysis (Fig. 2e and Supplementary Fig. 27). Such differences in electronic structures may thereby result in their different catalytic reactivity. According to the Arrhenius plots (Fig. 2f), the Ir₁/A-aUiO catalyst showed much lower apparent activation energy (E_{app}) for HCOOH evolution (9.8 kJ mol^{-1}) than Ir_x/A-aUiO (25.1 kJ mol^{-1}) and IrNPs/A-aUiO (55.6 kJ mol^{-1}), suggesting the much faster CO₂RR kinetics on Ir₁/A-aUiO under similar conditions. Thus, the SMSI could substantially modulate the electronic structures of Ir species, and the positively charged Ir SAs presented the best CO₂RR activity and selectivity targeting HCOOH production.

The reaction route for CO₂RR on the Ir₁/A-aUiO catalyst was further studied by isotope-labeled mass spectroscopy (MS) and in situ Fourier-transform infrared spectroscopy (FTIR). As revealed by the electrospray ionization-mass spectrometry (ESI-MS) (Supplementary Fig. 28), H¹³COO⁻ was the only reduction product when ¹³CO₂ was used as feed gas, confirming that the formates were generated from photocatalytic CO₂RR exclusively. Additionally, as shown in Supplementary Fig. 29, FTIR peaks (at 1497 and 1433 cm⁻¹) of the surface carbonic acid species^{36,37}, the intermediate species for formic acid evolution³⁶, were immediately observed when humidified CO₂ was fed into the reactors containing Ir₁/A-aUiO or A-aUiO catalysts in dark, indicating the adsorption of CO₂ by the hydroxyls on the Zr–O nodes of A-aUiO^{38,39}. The reactors were then purged with Ar to remove the excess CO₂. Under visible light irradiation, new infrared peaks (at 2920, 2850, and 1576 cm⁻¹) were observed on the Ir₁/A-aUiO catalyst (Supplementary Fig. 30a), suggesting the formation of HCOO* species upon irradiation^{40–42}. To the contrary, no significant HCOO* peaks could be found in the FTIR spectra for the bare A-aUiO particles (Supplementary Fig. 30b). In addition, as shown in Supplementary Fig. 17, the conduction band of A-aUiO (–0.60 V vs. NHE) is located more negative than the standard electrode potential of CO₂/HCOOH (–0.37 V vs. NHE)⁴³. Therefore, a plausible reaction route for photocatalytic CO₂RR on Ir₁/A-aUiO would be: the CO₂ molecules were first adsorbed by the A-aUiO to form surface carbonic acid species, and then hydrogenated on the Ir₁ catalytic centers with photogenerated electrons provided by the A-aUiO matrix and protons (from water) to form HCOOH^{44,45}. Meanwhile, the photo-generated holes could be reduced by the sacrifice agent (i.e., isopropanol, Supplementary Fig. 31) to facilitate the transfer of electrons to reduce CO₂ species. Interestingly, similar photocatalytic CO₂RR route for HCOOH production can be also enabled on other Ir₁/MOF catalysts. For instance, NH₂-MIL-125 (Ti) ref. ⁴⁶ (aMIL) decorated by Ir SAs (Ir₁/aMIL, Supplementary Fig. 32) showed significantly higher CO₂RR activity than the pristine aMIL components. Under visible light irradiation, the HCOOH evolution rates were 0.27 and 0.013 mmol g_{cat}⁻¹ h⁻¹, with the E_{app} of 20.1 and 58.7 kJ mol⁻¹ on Ir₁/aMIL and bare aMIL, respectively (Fig. 2g and Supplementary Fig. 33). Therefore, the synergy between the MOF matrix and the Ir SA active

centers contributes to CO₂RR for HCOOH evolution with high activity and selectivity.

Reaction interface design. Along with the catalytic center optimization, fabricating porous SA/MOF membranes allows us to build novel gas–solid reaction interfaces that can break the mass transfer limitation for gas reactants to further promote CO₂RR. Compared with the PiS mode in which the CO₂ availability in the vicinity of catalyst surfaces is restricted by their low solubility and sluggish diffusion in aqueous solutions (Fig. 3a), the updated gas-membrane-gas (GMG) (Fig. 3b, Supplementary Figs. 34, and 35) configuration can significantly decrease the diffusional lengths and resistance for gas reactants¹⁹. As a result, the molecular ratio of CO₂/H₂O in the vicinity of each catalytic centers can be increased by 4 orders of magnitude from 1/1600 (saturated CO₂ solutions, PiS) to ~30/1 (CO₂ gas with saturated H₂O steam, GMG)¹⁸. The increase of CO₂ availability and the reverse of CO₂/H₂O ratio in the SA/MOF membranes would thus dramatically enhance the CO₂RR activity in a wide range of CO₂ flow rates (Fig. 3d). For instance, with the CO₂ flow rate fixed at 120 standard cubic centimeters per minute (sccm), the Ir₁/A-aUiO membrane exhibited a HCOOH yield of $3.38 \text{ mmol g}_{\text{cat}}^{-1} \text{ h}^{-1}$ (i.e., 3.38 mmol of HCOOH per gram of Ir₁/A-aUiO catalysts per hour) in the GMG mode, exceeding more than six times that showed by Ir₁/A-aUiO particles ($0.51 \text{ mmol g}_{\text{cat}}^{-1} \text{ h}^{-1}$) in the PiS mode (Fig. 3d and Supplementary Table 2). The advantages for such catalyst and interface design were further demonstrated by the apparent quantum efficiency (AQE) measurements at various wavelengths. As shown in Supplementary Fig. 36, the Ir₁/A-aUiO membranes exhibited AQE values of 15.76 and 6.40% at 420 and 475 nm, respectively, which are much higher than that showed by the Ir₁/A-aUiO particles in the conventional PiS mode (2.51% and 1.10%, respectively). In addition, ESI-MS studies further indicated that the collected formates in the GMG mode were also exclusively generated by photocatalytic CO₂RR (Supplementary Fig. 37).

The advantages of the SA/MOF membranes and the high-throughput GMG reaction interfaces were further demonstrated by photocatalysis performances with different CO₂ availability. As shown in Fig. 3e, in the PiS mode, the HCOOH evolution rate increased gradually with the volume fractions of CO₂ concentrations in the mixture of CO₂ and Ar [i.e., CO₂/(CO₂ + Ar), v/v%]. To the contrary, the HCOOH yield increased rapidly and reached to the plateau at low CO₂ concentrations (<40 v/v%) in the GMG mode. Notably, in the relatively low CO₂ concentration region (<60 v/v%), the GMG configuration exhibited an order of magnitude higher HCOOH generation rate compared with the conventional PiS mode. These results further confirm that the Ir₁/A-aUiO membranes can enable efficient gas mass transfer, thereby enrich CO₂ with relatively low initial concentrations, and turn them into HCOOH with much higher efficiency than the powder catalysts dispersed in aqueous solutions. In addition, compared with the GMG mode, the identical 1.4 wt% Ir₁/A-aUiO membranes exhibited a much smaller formate yield of $0.76 \text{ mmol g}_{\text{cat}}^{-1} \text{ h}^{-1}$ in the spontaneous diffusion mode (Supplementary Fig. 38), where the mass transfer was driven by only spontaneous thermal motion of gaseous molecules^{24,25}. Therefore, addressing the mass transfer limitation encountered by the PiS mode (Fig. 3a) and the spontaneous diffusion mode (Supplementary Fig. 38), the Ir₁/A-aUiO membranes (GMG) exhibited near constant photocatalytic CO₂RR activity and selectivity ($3.38 \text{ mmol g}_{\text{cat}}^{-1} \text{ h}^{-1}$ and ~98% at the CO₂ flow rate of 120 sccm) through the long-term (100 h) operation (Fig. 3f), showing high stability with no significant changes observed in the recycled Ir₁/A-aUiO photocatalysts (Supplementary Fig. 39).

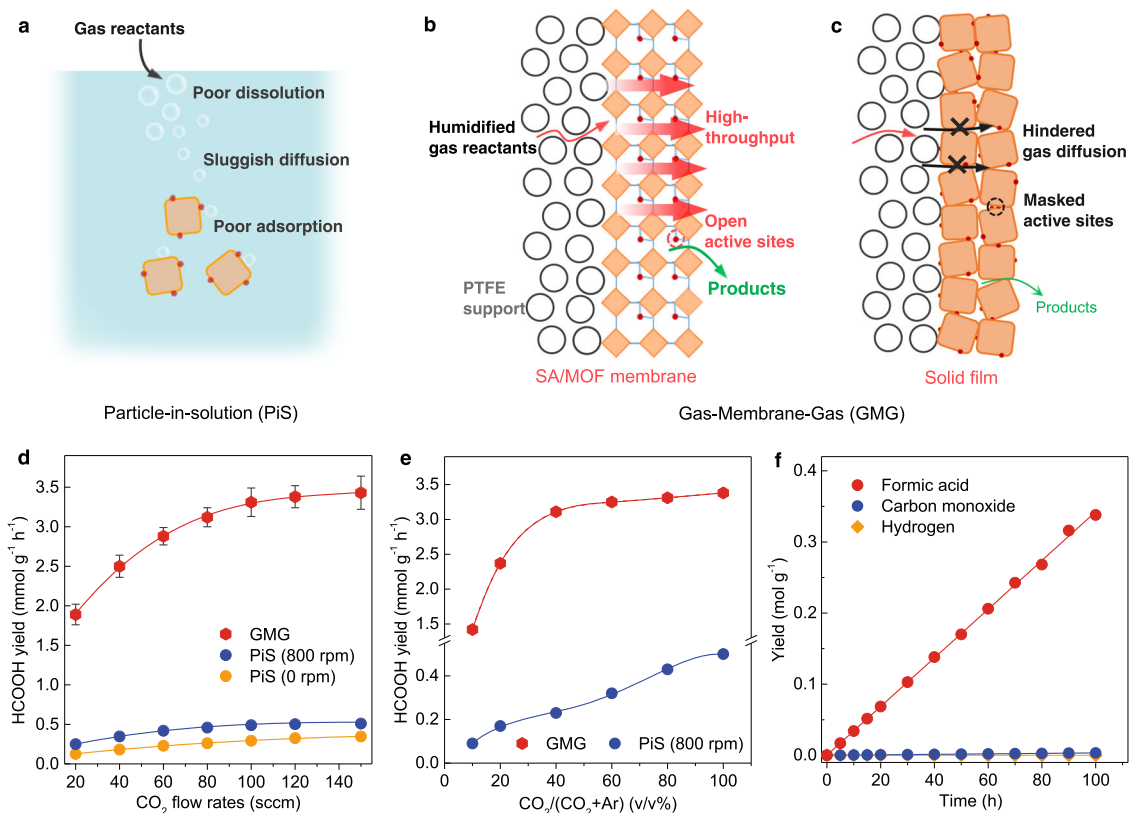


Fig. 3 Photocatalytic CO₂RR on SA/MOF membranes. **a** In the particle-in-solution (PiS) mode, gas-phase CO₂ was fed into the aqueous photocatalyst dispersion and then reduced on the water flooded surfaces of catalysts. **b** In the gas-membrane-gas (GMG) mode, humidified CO₂ gas was fed through the SA/MOF membrane, where water vapor was carried by the CO₂ stream. **c** Schematic illustration for the solid films fabricated by non-porous semiconductor particles. **d** HCOOH yields on Ir₁/A-aUiO particles (PiS) and membrane (GMG) under different CO₂ flow rates, respectively. **e** HCOOH yields on Ir₁/A-aUiO particles (PiS) and membrane (GMG) under different CO₂ concentration (in Ar mixtures), respectively. **f** Time course of HCOOH, CO and H₂ evolution on Ir₁/A-aUiO membrane (GMG). All the photocatalytic reactions were performed under visible light (>420 nm). The CO₂ flow rates in **e** and **f** were fixed at 120 sccm. Error bars represent the standard deviation for three independent catalysis tests.

Further control experiments suggested the vital role of the highly porous MOF matrix in constructing such high-throughput gas–solid catalytic interfaces. The porous Ir₁/A-aUiO and Ir₁/aMIL membranes exhibited a 5.6-fold and 4.8-fold enhancement in CO₂RR activity as compared with their powder counterparts, respectively; however, the solid films composed of non-porous inorganic particles (e.g., Ir/TiO₂, Ir/ZnO) showed a much lower activity enhancement (~40%) (Supplementary Figs. 40–44). These significant differences in enhancement factors for CO₂RR on MOF membranes, and solid films may arise from their markedly different mass transfer and photoelectron deliver efficiencies (Fig. 3b, c). Thanks to the high porosity and open pore structure of MOF matrixes, the diffusion of CO₂/H₂O molecules from gas phase to the highly dispersed active centers would be efficient in high throughput (Supplementary Fig. 45). The delivery of photoelectrons from the local ligands to the active sites also not be hindered by stacking SA/MOF particles. However, the aggregation of solid semiconductor particles would form a solid film that would retard the efficient diffusion of gas molecules to the surface active sites (Fig. 3c and Supplementary Fig. 45), further suppressing the photocatalytic reduction of CO₂ on such solid films.

The use of water vapor instead of aqueous solutions as proton sources brought additional advantages for CO₂RR. As shown in Supplementary Fig. 46, in the PiS mode, the HCOOH evolution rate significantly declined when tap water or rainwater (both collected on the BIT campus in Beijing) was used as proton

sources instead of the ultrapure DI water. The decrease in catalyst activity would be possibly caused by the impurities in tap water or rainwater (e.g., Cl⁻, ClO⁻ and other ions), which may poison the active centers. However, using the naturally purified water vapor as proton sources could effectively avoid the poisoning of catalyst from such impurities, and ensure the HCOOH yield despite the types of water sources. Therefore, our SA/MOF membranes and GMG interface designs exhibited great potential in fixing relatively low-concentration CO₂ to HCOOH with high selectivity and activity, using naturally available water as proton sources and visible light as energy supplies.

Photocatalytic oxygen reduction reaction. Notably, the wide applicability of our catalyst and reaction interface design strategy can be further applied to the photoreduction of O₂ to H₂O₂ (Fig. 4). Like Ir/A-aUiO, the strong metal-substrate interactions could also modulate the electronic structures of Pd species (e.g., Pd SAs, clusters, and nanoparticles) supported by A-aUiO matrix (Fig. 4a and Supplementary Figs. 47 and 48). As compared with the Pd clusters and nanoparticles, the positively charged Pd₁ sites could not only significantly promote H₂O₂ generation but also effectively suppress H₂O₂ decomposition⁴⁷ (Fig. 4b and Supplementary Fig. 49). As a result, in the PiS mode, Pd₁/A-aUiO particles exhibited an H₂O₂ yield (1.74 mmol g_{cat}⁻¹ h⁻¹) that was more than 3 and 12 times that of Pd_x/A-aUiO (0.58 mmol g_{cat}⁻¹ h⁻¹) and PdNPs/A-aUiO (0.14 mmol g_{cat}⁻¹ h⁻¹),

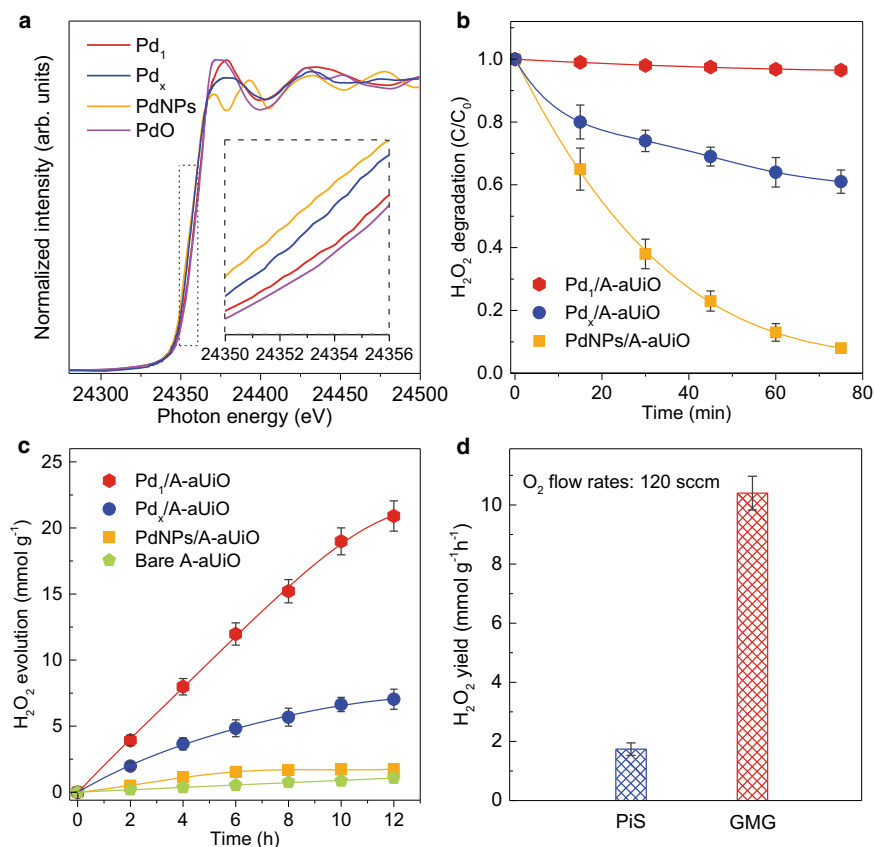


Fig. 4 Photocatalytic O₂ reduction (ORR) on Pd modified MOF powders and membrane. **a** Pd K-edge XANES spectra of PdNPs, Pd_x, and Pd₁ decorated A-aUiO catalysts. PdO was used as standard. **b** Time course of H₂O₂ decomposition on PdNPs, Pd_x, and Pd₁ decorated A-aUiO catalysts. **c** Time course of H₂O₂ generation on pristine A-aUiO and PdNPs, Pd_x, and Pd₁ decorated A-aUiO catalysts. **d** H₂O₂ yields on Pd₁/A-aUiO particles (PiS) and membranes (GMG), respectively. All the photocatalytic reactions were performed under visible light (>420 nm) irradiation and using isopropanol (20 v/v% in water) as sacrificial agents. The O₂ flow rates were fixed at 120 sccm. Error bars represent the standard deviation for three independent catalysis tests.

respectively (Fig. 4c). Additional control experiments confirmed that the detected H₂O₂ was produced by reducing O₂ exclusively. As shown in Supplementary Fig. 50, no H₂O₂ production could be detected in experiments without light irradiation, O₂ feed, or catalysts (i.e., Pd₁/A-aUiO). Like the CO₂RR case, further enhancement in H₂O₂ generation activity could be realized by reacting humidified O₂ gas flow on Pd₁/A-aUiO membrane in the GMG mode, showing a high H₂O₂ evolution rate (10.4 mmol g_{cat}⁻¹ h⁻¹) that was more than 4.9-fold higher than that observed in the PiS mode (Fig. 4d and Supplementary Table 3). That is, the gas-permeable MOF (e.g., A-aUiO, aMIL) membranes can serve as a versatile array of photosensitizer and nanoreactor to host different metal SAs (e.g., Ir, Pd), for the selective photocatalytic reduction of specific gases into chemical fuels under visible light and mild conditions.

The highly porous SA/MOF membranes decorated with single-atomic reaction centers, assembling numerous regularly arranged and interconnected photocatalytic nanoreactors, bridge the best of homogeneous and heterogeneous catalysis. On one hand, like molecular catalysts, the explicit structures for the highly dispersed photocatalytic modules (ligand–node–SA) allow us to modify their light harvesting, electron delivery, and catalytic conversion properties with atomic precision. On the other hand, the porous but rigid MOF crystals hold all the nanoreactors together via stable coordination bonds with interconnected pores, ensuring the high stability, dispersity, and accessibility of the atomically dispersed catalytic centers. Especially, starting with humidified gas instead of gas solutions, the novel GMG reaction interfaces not only facilitate the diffusion of gas molecules but also eliminate

the competitive adsorption of liquid water, which is inevitable in conventional three-phase photocatalytic gas reduction reactions. The substantial increase in local concentration and molar ratio of gas reactants in the vicinity of each catalytic center, thereby promote the activity and selectivity of photocatalytic reduction of gas molecules significantly.

In practice, our SA/MOF membranes can directly reduce CO₂ and O₂ into value-added and ready-to-use chemical fuels (i.e., HCOOH and H₂O₂). With specifically designed catalytic centers, the major components of air (CO₂, O₂, and even N₂) could be fixed via sustainable photocatalytic reactions, with water vapor as proton donors under mild conditions to convert and store the intermittent solar energy. The facile preparation of SA/MOF membranes facilitates the scale-up of such photocatalysis devices, and the minimized usage of water vapor saves the cost of freshwater in arid regions with rich solar powers. Our work provides a general and programmable strategy bridging photocatalysis center, and reaction interface designs to solve the complexity for mass transfer and catalytic conversion in three-phase photocatalytic reactions. The powerful toolbox in single-atom and MOF chemistry endows us with almost infinite possibilities to engineer the chemical structures of SA/MOF membranes. Such design may find wider applicability in more substantial heterogeneous reactions.

Methods

Preparation of NH₂-UiO-66 (aUiO) particles. In a typical synthesis, 10 mg of anhydrous zirconium chloride (ZrCl₄) was dissolved in 5 mL of N,N-Dimethylformamide (DMF) in a 20 mL glass vial. In another vial, 15 mg of 2-

aminoterephthalic acid ($\text{NH}_2\text{-BDC}$) was also dissolved in 5 mL of DMF. Then, the two solutions were mixed before 1.3 mL of acetic acid was added. The resulting solution was shaken and then heated in a 120 °C isothermal for 12 h. Light yellow powders were collected by centrifugation, washed five times with DMF over a period of 48 h, and five times with methanol over a period of 36 h. Finally, light yellow aUiO powder was obtained by drying the products under the dynamic vacuum overnight at room temperature.

Preparation of defect-rich $\text{NH}_2\text{-UiO-66}$ (A-aUiO) particles. The as-prepared aUiO powders with partial acetate ligands were activated under high dynamical vacuum and high temperature to remove the acetate residuals and obtain A-aUiO. Typically, 120 mg of the as-prepared aUiO powders were put into a quartz crucible and kept in a vacuum oven at 100 °C for 8 h. Then, the oven temperature was raised to 180 °C at a rate of 2 °C min^{-1} and maintained at 180 °C for 28 h. Finally, brownish yellow powder was obtained after cooling down to room temperature.

Preparation of $\text{Ir}_1/\text{A-aUiO}$ (1.4 wt%). In a typical synthesis, 80 mg of A-aUiO powders were fully dispersed by 60 mL of ultrapure water. Then, under vigorous stirring, 1.3 mL of K_2IrCl_6 solution (5 mM) was slowly injected (1 mL min^{-1}) into the above dispersion with an injection pump. The mixture was stirred at 500 rpm under 40 °C for 12 h. After that, the products were collected via centrifugation and washed by ultrapure water. After drying in the vacuum oven under 80 °C, the products were put into a quartz boat and heated to 200 °C at a rate of 5 °C min^{-1} and maintained at 200 °C for 1 h in a tubular oven under high-purity (99.9999%) Ar protection (60 sccm). The resultant powders were cooled down to room temperature and collected for further characterizations and tests. The preparation of 0.7 wt% $\text{Ir}_1/\text{A-aUiO}$ particles was similar but with K_2IrCl_6 solution of lower concentration (2.5 mM).

Preparation of $\text{Ir}_x/\text{A-aUiO}$. In a typical synthesis, 60 mg of A-aUiO powders were fully dispersed by 45 mL of ultrapure water. Then, 1.3 mL of K_2IrCl_6 solution (7.5 mM) was injected (1 mL min^{-1}) into the above dispersion with an injection pump. The mixture was stirred at 500 rpm under 40 °C for 12 h. After that, the products were collected via centrifugation and washed by ultrapure water (two times). After drying in the vacuum oven under 80 °C, the products were put into a quartz boat and heated to 250 °C at a rate of 5 °C min^{-1} and maintained at 250 °C for 1 h in a tubular oven under H_2/Ar (1/4 v/v, 60 sccm).

Preparation of $\text{IrNPs}/\text{A-aUiO}$. In a typical synthesis, 60 mg of A-aUiO powders were fully dispersed in 45 mL of ultrapure water. Then, 1.3 mL of K_2IrCl_6 solution (15 mM) was injected into the above dispersion. The mixture was stirred at 500 rpm under room temperature for 1 h. After that, the products were collected via centrifugation and washed by ultrapure water. After drying in the vacuum oven under 80 °C, the products were put into a quartz boat and heated to 300 °C at a rate of 5 °C min^{-1} and maintained at 300 °C for 2 h in a tubular oven under H_2/Ar (1/4 v/v, 60 sccm).

Preparation of Ir_1/aMIL . Typically, 655 mg of $\text{NH}_2\text{-BDC}$, 6.5 mL of anhydrous DMF, 1.2 mL of anhydrous methanol and 0.312 mL of $\text{Ti}(\text{O}i\text{Pr})_4$ were added into a 15 mL Teflon-lined autoclave. After 0.5 h of sonication, the autoclave was sealed and heated at 130 °C for 15 h. Light yellow powders were collected by centrifugation, washed five times with DMF over a period of 48 h, and five times with methanol over a period of 24 h. Finally, $\text{MIL-125}(\text{NH}_2)$ (aMIL) powders were obtained by drying and activating under 160 °C and dynamic vacuum for 24 h. After that, 80 mg of the activated aMIL powders were dispersed by 60 mL of ultrapure water. Then, under vigorous stirring, 1.3 mL of K_2IrCl_6 solution (5 mM) was injected (1 mL min^{-1}) into the above dispersion with an injection pump. The mixture was stirred at 500 rpm under 40 °C for 12 h. The products were collected via centrifugation and washed by ultrapure water (two times). After drying in the vacuum oven under 80 °C, the product was put into a quartz boat and heated to 200 °C at a rate of 5 °C min^{-1} , and maintained at 200 °C for 1 h in a tubular oven under high-purity (99.9999%) Ar protection (60 sccm).

Preparation of $\text{Pd}_1/\text{A-aUiO}$. Eighty milligram of A-aUiO powders were fully dispersed in 60 mL of ultrapure water. Then, 1.3 mL of Na_2PdCl_4 aqueous solution (5 mM) was slowly injected (0.5 mL/min) into the above dispersion with an injection pump. The mixture was then stirred under room temperature for 14 h. After that, the products were collected via centrifugation and washed by ultrapure water (two times). After drying in the vacuum oven under 80 °C, the products were put into a quartz boat and heated to 200 °C at a rate of 5 °C min^{-1} and maintained at 200 °C for 1 h in a tubular oven under high-purity (99.9999%) Ar protection (60 sccm). The resultant powders were cooled down to room temperature and collected for further characterizations and tests.

Preparation of $\text{Pd}_x/\text{A-aUiO}$. Sixty milligram of A-aUiO powders were fully dispersed in 60 mL of ultrapure water. Then, 1.3 mL of Na_2PdCl_4 aqueous solution (7.5 mM) was slowly injected (1 mL/min) into the above dispersion with an injection pump. The mixture was then stirred under room temperature for 14 h.

After that, the products were collected via centrifugation and washed by ultrapure water (two times). After drying in the vacuum oven under 80 °C, the products were put into a quartz boat and heated to 200 °C at a rate of 5 °C min^{-1} and maintained at 200 °C for 1 h in a tubular oven under high-purity (99.9999%) Ar protection (60 sccm). The resultant powders were cooled down to room temperature and collected for further characterizations and tests.

Preparation of $\text{PdNPs}/\text{A-aUiO}$ (1.3 wt%). In a typical synthesis, 60 mg of A-aUiO powders were fully dispersed in 45 mL of ultrapure water. Then, 1.3 mL of Na_2PdCl_4 solution (15 mM) was injected into the above dispersion. The mixture was stirred at 500 rpm under room temperature for 1 h. After that, the products were collected via centrifugation and washed by ultrapure water. After drying in the vacuum oven under 80 °C, the products were put into a quartz boat and heated to 300 °C at a rate of 5 °C min^{-1} and maintained at 300 °C for 2 h in a tubular oven under H_2/Ar (1/4 v/v, 80 sccm).

Preparation of Ir/TiO_2 (0.42 wt%) and Ir/ZnO (0.40 wt%). Sixty milligram of commercially available TiO_2 (Acros) or ZnO (Acros) powders were fully dispersed in 45 mL ultrapure water. Then, 1.3 mL of K_2IrCl_6 aqueous solution (5 mM) was slowly injected into the above dispersion. The mixture was then stirred at 500 rpm under room temperature for 12 h. After drying in the vacuum oven under 80 °C, the products were put into a quartz boat and heated to 300 °C at a rate of 5 °C min^{-1} and maintained at 300 °C for 1 h in a tubular oven under high-purity (99.9999%) Ar protection (60 sccm). The resultant powders were cooled down to room temperature and collected for further characterizations and tests.

Fabrication of leaf-like SA/MOF membranes. Typically, 12.5 mg of SA/MOF powders ($\text{Ir}_1/\text{A-aUiO}$, $\text{Pd}_1/\text{A-aUiO}$ or Ir_1/aMIL) were first dispersed in a mixture of isopropanol, ultrapure water and Nafion solution (150 μL of Nafion solution in 8 mL of 7:1 isopropanol:water mixture). The mixture was then sonicated for 30 min to produce SA/MOF inks. Then the inks were deposited onto one side of commercially available polytetrafluoroethylene (PTFE) films to fabricate the 15- μm -thick membranes through vacuum filtration. After that, the as-prepared membranes were dried in Ar and activated in high dynamical vacuum at 80 °C.

Fabrication of TiO_2 and ZnO -based solid films. About 20 mg of Ir/TiO_2 or Ir/ZnO powders were dispersed in a mixture of isopropanol, water, and Nafion solution (150 μL of Nafion solution in 8 mL of 7:1 isopropanol:water mixture). The mixture was then sonicated for 1.5 h to produce catalysts inks. Then the inks were deposited onto one side of the polytetrafluoroethylene (PTFE) films to fabricate the 15- μm -thick membranes through vacuum filtration. After that, the as-prepared membranes were dried in vacuum under 80 °C.

Characterization. XRD measurements of the obtained catalyst powders were performed on a Rigaku MiniFlex 600 diffractometer with a Cu-K α X-ray radiation source ($\lambda = 0.154056$ nm). Typically, 2 mg of powders were placed on an amorphous silica substrate and the XRD patterns were recorded at a scan rate of 2° min^{-1} . XPS measurements were performed by a Thermo VEG ESCALAB-250 system with Al-K α and Mg-K α source operated at 15 kV. The binding energies were referred to the C 1s peak (284.8 eV) from adventitious carbon. In situ FTIR spectra were recorded a Bruker ALPHA spectrometer. The one-dimensional ^1H spectra were recorded on Bruker ARX-400 and Bruker ARX-700 spectrometers. ESI-MS results were recorded on a PE SCIEX API 150 mass spectrometer. In the tests, the solution was continuously infused with a syringe pump at a constant flow rate into the pneumatically assisted electrospray probe with N_2 as the nebulizing gas. N_2 sorption isotherms were measured at 77 K on a Quantachrome ASiQM-VH002-5 absorption apparatus. Before tests, the samples were pre-activated at 120 °C for 12 h. The pore size distributions were estimated by the DFT method from a N_2 sorption experiment at 77 K. The metal loading in our catalysts was determined by an ICP-AES spectrometer (Model Optima 2000, PerkinElmer). A series of solutions for the measurements were prepared by dissolving 20 mg of samples in 4 mL of aqua regia (75 vol.% HCl and 25 vol.% HNO_3). The solution was left overnight to allow complete dissolution. The resultant solution was diluted to 50 mL with deionized water in a volumetric flask and then analysed using ICP-AES. UV-Vis DRS spectra were recorded by a UV-2600 (Shimadzu) spectrophotometer in the wavelength range of 300–800 nm, using BaSO_4 as reference. The steady-state PL spectra were measured by an F-4500 spectrophotometer (Hitachi). The transient-state PL spectra were carried out on an FLSP920 spectrophotometer (Edinburgh Instruments). The ESR measurements were performed out on a JEOL FA-200 micro spectrometer at 90 K. Samples were placed into NMR tubes and cooled to 90 K using liquid nitrogen stream for measurements.

The TEM images were obtained on a JEM-2100 transmission electron microscope operating at 200 kV. The samples were prepared by dropping water/ethanol dispersion of samples onto ultrathin carbon film and immediately evaporating the solvent. The high-angle annular dark-field scanning TEM (HAADF-STEM) images were obtained on a TECNAI F30 transmission electron microscope operating at 300 kV. The aberration-corrected high-angle annular dark-field scanning TEM (AC-HAADF-STEM) images and STEM-EDX elemental mapping were collected on a JEM-ARM200F transmission electron microscopy

working at 200 kV, equipped with a probe spherical aberration corrector. The SEM images and EDX elemental mapping were acquired from JEOL S-4800 and Zeiss Supra 55 scanning electron microscopes.

The Ir L-edge XAFS spectra were obtained at beamline BL14W1 of the Shanghai Synchrotron Radiation Facility (SSRF). The samples were measured in fluorescence mode by using a 32-element Ge solid state detector to collect the data. Iridium foil (Ir), iridium chloride (IrCl₃), and iridium oxide (IrO₂) were used as standard reference materials for these measurements. The Pd K-edge XAFS spectra were obtained at beamline BL14W1 of the Shanghai Synchrotron Radiation Facility (SSRF), and beamline BL01C1 of the National Synchrotron Radiation Research Center (NSRRC). The samples were measured in fluorescence mode by using a solid-state detector to collect the data. Palladium foil (Pd), and palladium oxide (PdO) were used as standard reference materials for these measurements. Athena and Artemis codes were used to extract the data and fit the profiles. For the X-ray absorption near edge structure (XANES) part, the experimental absorption coefficients as function of energies $\mu(E)$ were processed by background subtraction and normalization procedures and reported as “normalized absorption” for all the measured samples and standard references. For the extended X-ray absorption fine structure (EXAFS) part, the Fourier transformed (FT) data in R space were analyzed by applying different models for M–O, M–Cl and M–M (M = Ir, Pd) contributions. The passive electron factors, S_0^2 , were determined by fitting the experimental data on metal foils and fixing the coordination number (CN) of M–M, and then fixed for further analysis of the measured samples. The parameters describing the electronic properties (e.g., correction to the photoelectron energy origin, E_0) and local structure environment including CN, bond distance (R), and Debye–Waller factor around the absorbing atoms could vary during the fit process.

Photocatalytic CO₂RR in the conventional particle-in-solution (PiS) mode. The photocatalytic CO₂ reduction reaction (CO₂RR) experiments were carried out in an outer irradiation-type photo-reactor (Pyrex glass) connected to a closed gas-circulation system (Supplementary Fig. 21). High-purity CO₂ (99.9999%) was cycled by a gas-recycle-pump with tunable flow rates. Typically, 15 mg of catalyst powders were dispersed in a mixture of water and isopropanol (40 mL of water and 10 mL of isopropanol). The dispersion was transferred into the catalysis system, thoroughly degassed to remove the air by high-purity Ar (99.9999%) displacement. After 30 min of high-purity (99.9999%) CO₂ bubbling, the dispersion was illuminated by a 300 W Xe-lamp (Beijing China Education Au-light Co., Ltd.) with a 420 nm long-pass filter. During the catalysis tests, the CO₂ was continuously bubbled at the flow rate of 120 mL min⁻¹ into the dispersion, which was magnetically stirred at 800 rpm. The liquid products (e.g., HCOOH) were quantified with NMR. Typically, after photocatalytic CO₂RR, 500 μ L of the resultant solution was extracted from the reactor and mixed with 100 μ L of D₂O (99.9 at % D, Sigma-Aldrich) containing 0.05 μ L of dimethyl sulfoxide (99.9%, Sigma-Aldrich), as an internal standard. The ¹H NMR spectra were then measured with water suppression using a pre-saturation method. The gaseous products were quantified by an online gas chromatography (Shimadzu GC-2014C) with a packed column (MS-13X). A thermal conductivity detector (TCD) was used to quantify H₂ concentration, and a flame ionization detector (FID) with a methanizer was used to quantitatively analyze the content of CO.

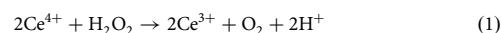
Photocatalytic CO₂RR in the GMG mode. The photocatalytic CO₂RR tests of the leaf-like membranes in the GMG mode were carried out in a home-made outer irradiation-type gas-flow cell connected to a closed gas-circulation system (Supplementary Fig. 34). The as-prepared membranes were sandwiched by two gas chambers (Supplementary Fig. 35). During the photocatalysis process, humidified high-pure CO₂ (99.9999%) was cycled continuously in the whole system by a gas-recycle-pump with tunable flow rates, so that the CO₂ and water molecules could continuously pass across the membranes. Before tests, the whole catalytic system was thoroughly degassed to remove the air by high-purity Ar (99.9999%) displacement. After 30 min of high-purity (99.9999%) CO₂ circulation, the membranes were illuminated by a 300 W Xe-lamp (Beijing China Education Au-light Co., Ltd.) with a 420 nm long-pass filter. The water vapor carried liquid products (e.g., HCOOH) were collected by a cold trap and then quantified with NMR. The gas-phase products (e.g., H₂) were quantified by an online gas chromatography (Shimadzu GC-2014C).

Photocatalytic CO₂RR in the spontaneous diffusion mode. The photocatalytic CO₂RR tests of the 1.4 wt% Ir₁/A-aUiO membranes in the spontaneous diffusion mode were carried out following previously reported procedures²⁵. Before reaction, the Ir₁/A-aUiO membrane with the effective geometric area of ~12.5 cm² was placed horizontally in the center of an air-tight reaction cell (400 mL). Then, the air inside the reaction cell was evacuated before the cell was filled with ultra-pure CO₂. This vacuum and refill procedure was repeated three times to remove the air residuals in the reactor. After another 30 min for the establishing of an adsorption-desorption balance, 3 mL of ultrapure H₂O was added to the reactor (without direct contact with the membrane) to provide humidity. A 300 W Xe lamp with a 420 nm long-pass filter was employed as a light source to illuminate the catalyst membrane from the top of the reactor. After 2 h of irradiation, the reaction cell was further heated to 60 °C to ensure the generated HCOOH was fully

gasified, the water vapor carried HCOOH were then collected by a cold trap and quantified with NMR.

Photocatalytic O₂ reduction in the conventional particle-in-solution (PiS) mode.

The photocatalysis O₂ reduction reaction (ORR) tests were also carried out in an outer irradiation-type photoreactor (Pyrex glass) connected to a closed gas-circulation system. High-purity O₂ (99.9999%) was cycled by a gas-recycle-pump with tunable flow rates. Typically, 20 mg of the photocatalyst powders were dispersed in a mixture of water (40 mL) and isopropanol (10 mL). The dispersion was transferred into the catalysis system, thoroughly degassed to remove the air by high-purity Ar (99.9999%) displacement. After 30 min of high-purity (99.9999%) O₂ bubbling, the dispersion was illuminated by a 300 W Xe-lamp (Beijing China Education Au-light Co., Ltd.) with a 420 nm long-pass filter. During the photocatalytic tests, the O₂ was continuously bubbled at the flow rate of 120 mL min⁻¹ into the dispersion, which was magnetically stirred at 800 rpm. The H₂O₂ decomposition reactions were carried out in a Pyrex glass vial. Twenty milligram of the catalyst powders were dispersed in a mixture of hydrogen peroxide (50 μ mol), water (40 mL) and isopropanol (10 mL). The dispersion was transferred into the catalysis system, thoroughly degassed to remove the air by high-purity Ar (99.9999%) displacement. After that, the catalysis reactions were carried out under visible light irradiation. During the tests, the Ar was continuously bubbled at the flow rate of 30 mL min⁻¹ into the dispersion, which was magnetically stirred at 800 rpm. The H₂O₂ concentration was measured by a cerium sulfate Ce(SO₄)₂ titration method based on the mechanism, that the yellow solution of Ce⁴⁺ could be reduced to colorless Ce³⁺ by H₂O₂ according to the following equation:



Thus, the concentration of H₂O₂ could be obtained by measuring the concentration of Ce⁴⁺ (UV–Visible absorption at the wavelength of 316 nm) ref. ⁴⁸.

Photocatalytic O₂ reduction in the GMG mode. The photocatalytic O₂ reduction tests of the leaf-like membranes in the GMG mode were also carried out in a home-made outer irradiation-type gas-flow cell connected to a closed gas-circulation system. The as-prepared membranes were sandwiched by two gas chambers. During the catalysis process, humidified high-purity O₂ (99.9999%) was cycled continuously in the whole system by a gas-recycle-pump with tunable flow rates, so that the O₂ and water molecules could continuously pass across the membranes. In addition, the surfaces of the leaf-like membranes needed to be washed by ultrapure water (was cycled by a peristaltic pump) intermittently (with a fixed interval of 20 min) to ensure the efficient collection of the liquid H₂O₂ generated during the catalytic process. Before tests, the whole catalytic system was thoroughly degassed to remove the air by high-purity Ar (99.9999%) displacement. After 30 min of high-purity (99.9999%) O₂ circulation, the membranes were illuminated by a 300 W Xe-lamp (Beijing China Education Au-light Co., Ltd.) with a 420 nm long-pass filter.

AQE for formate production at different wavelength. The calculation of the AQE followed the standard procedure of photocatalytic reactions. In detail, the AQE was obtained by performing CO₂RR under monochromatic light using appropriate bandpass filters at different wavelengths (e.g., 380, 400, 420, 450, 475, 500, 520, 550, 575, and 600 nm). The power intensity of the monochromatic light was measured using an optical power meter (CEL-NP2000, Beijing China Education Au-light Company Limited, China). The calculation of AQE was based on:

$$\text{AQE} = \frac{N_{\text{reacted}}}{N_{\text{incident}}} \times 100\% \quad (2)$$

In the above equation, N_{reacted} and N_{incident} are the number of the reacted and incident photons, respectively, which can be obtained from:

$$N_{\text{reacted}} = 2 \times N_A \times n_{\text{HCOOH}}, \quad (3)$$

$$N_{\text{incident}} = \frac{Pt}{hv} = \frac{ISt\lambda}{hc}, \quad (4)$$

where N_A is the Avogadro constant ($6.022 \times 10^{23} \text{ mol}^{-1}$), n_{HCOOH} is the amount of the produced HCOOH molecules (in mol), P is the light power (W), t is the illumination time (s), h is the Planck constant ($6.626 \times 10^{-34} \text{ J s}$), ν is light frequency (Hz), I is the light intensity (W cm^{-2}), S is the irradiated area (cm^2), λ is wavelength of monochromatic light (m), and c is the speed of light in free space ($3.0 \times 10^8 \text{ m s}^{-1}$).

Photo-electrochemical measurements. Photo-electrochemical tests were performed using a CHI 660E potentiostat with a three-electrode system. A platinum plate ($1 \times 1 \text{ cm}^2$), a saturated calomel electrode (SCE), and a modified fluorine-doped tin oxide (FTO) glass plate ($1 \times 2 \text{ cm}^2$) were used as the counter, reference, and working electrode, respectively. All potentials in this study were measured against the SCE and converted to the reversible hydrogen electrode

(RHE) reference scale by

$$E(\text{V vs. RHE}) = E(\text{V vs. SCE}) + 0.0591 \times \text{pH} + 0.244 \quad (5)$$

To prepare working electrodes, 15 mg of catalyst powders were dispersed in the mixed solution of 2 mL of water, 0.7 mL of ethanol and 0.3 mL of 5 wt% Nafion by sonication for at least 30 min to form a homogeneous ink. Then, 150 μL of the as-prepared catalyst inks were loaded onto the FTO electrode and dried under room temperature.

Data availability

All data that support the plots and other findings within this paper are available from the corresponding authors on reasonable request. Source data are provided with this paper.

Received: 8 September 2020; Accepted: 7 April 2021;

Published online: 11 May 2021

References

- Larkum, A. Limitations and prospects of natural photosynthesis for bioenergy production. *Curr. Opin. Biotechnol.* **21**, 271–276 (2010).
- Atsumi, S., Higashide, W. & Liao, J. C. Direct photosynthetic recycling of carbon dioxide to isobutyraldehyde. *Nat. Biotechnol.* **27**, 1177–1180 (2009).
- Sakimoto, K. K., Wong, A. B. & Yang, P. D. Self-photosensitization of nonphotosynthetic bacteria for solar-to-chemical production. *Science* **351**, 74–77 (2016).
- Ran, J. R., Jaroniec, M. & Qiao, S. Z. Cocatalysts in semiconductor-based photocatalytic CO₂ reduction: achievements, challenges, and opportunities. *Adv. Mater.* **30**, 1704649 (2018).
- Kornienko, N., Zhang, J. Z., Sakimoto, K. K., Yang, P. D. & Reisner, E. Interfacing nature's catalytic machinery with synthetic materials for semi-artificial photosynthesis. *Nat. Nanotechnol.* **13**, 890–899 (2018).
- Li, A. et al. Three-phase photocatalysis for the enhanced selectivity and activity of CO₂ reduction on a hydrophobic surface. *Angew. Chem. Int. Ed.* **58**, 14549–14555 (2019).
- Li, X. D. et al. Selective visible-light-driven photocatalytic CO₂ reduction to CH₄ mediated by atomically thin CuIn₂S₆ layers. *Nat. Energy* **4**, 690–699 (2019).
- Dai, C. H. et al. Triphenylamine based conjugated microporous polymers for selective photoreduction of CO₂ to CO under visible light. *Green. Chem.* **21**, 6606–6610 (2019).
- Lin, R. X. et al. Monolithic all-perovskite tandem solar cells with 24.8% efficiency exploiting comproportionation to suppress Sn(II) oxidation in precursor ink. *Nat. Energy* **4**, 864–873 (2019).
- Cestellos-Blanco, S., Zhang, H., Kim, J. M., Shen, Y. X. & Yang, P. D. Photosynthetic semiconductor biohybrids for solar-driven biocatalysis. *Nat. Catal.* **3**, 245–255 (2020).
- Gao, C., Wang, J., Xu, H. X. & Xiong, Y. J. Coordination chemistry in the design of heterogeneous photocatalysts. *Chem. Soc. Rev.* **46**, 2799–2823 (2017).
- Rao, H., Schmidt, L. C., Bonin, J. & Robert, M. Visible-light-driven methane formation from CO₂ with a molecular iron catalyst. *Nature* **548**, 74–77 (2017).
- Ma, B. et al. Efficient visible-light-driven CO₂ reduction by a cobalt molecular catalyst covalently linked to mesoporous carbon nitride. *J. Am. Chem. Soc.* **142**, 6188–6195 (2020).
- Zhang, L. W. et al. Direct observation of dynamic bond evolution in single-atom Pt/C₃N₄ catalysts. *Angew. Chem. Int. Ed.* **59**, 6224–6229 (2020).
- Huang, P. P. et al. Selective CO₂ reduction catalyzed by single cobalt sites on carbon nitride under visible-light irradiation. *J. Am. Chem. Soc.* **140**, 16042–16047 (2018).
- Zhong, W. F. et al. A covalent organic framework bearing single Ni sites as a synergistic photocatalyst for selective photoreduction of CO₂ to CO. *J. Am. Chem. Soc.* **141**, 7615–7621 (2019).
- Hu, Y. G. et al. Tracking mechanistic pathway of photocatalytic CO₂ reaction at Ni sites using operando, time-resolved spectroscopy. *J. Am. Chem. Soc.* **142**, 5618–5626 (2020).
- Li, J. et al. Efficient electrocatalytic CO₂ reduction on a three-phase interface. *Nat. Catal.* **1**, 592–600 (2018).
- Tan, Y. C., Lee, K. B., Song, H. & Oh, J. H. Modulating local CO₂ concentration as a general strategy for enhancing C–C coupling in CO₂ electroreduction. *Joule* **4**, 1104–1120 (2020).
- Goyal, A., Marcondalli, G., Mints, V. A. & Koper, M. T. M. Competition between CO₂ reduction and hydrogen evolution on a gold electrode under well-defined mass transport conditions. *J. Am. Chem. Soc.* **142**, 4154–4161 (2020).
- Bhosale, S. S. et al. Mechanism of photocatalytic CO₂ reduction by bismuth-based perovskite nanocrystals at the gas-solid interface. *J. Am. Chem. Soc.* **141**, 20434–20442 (2019).
- Wu, X. Y. et al. Photocatalytic CO₂ conversion of M_{0.33}WO₃ directly from the air with high selectivity: insight into full spectrum induced reaction mechanism. *J. Am. Chem. Soc.* **141**, 5267–5274 (2019).
- Liang, L. et al. Infrared light-driven CO₂ overall splitting at room temperature. *Joule* **2**, 1004–1016 (2018).
- Li, R. et al. Integration of an inorganic semiconductor with a metal-organic framework: a platform for enhanced gaseous photocatalytic reactions. *Adv. Mater.* **26**, 4783–4788 (2014).
- Jiang, Z. et al. Filling metal-organic framework mesopores with TiO₂ for CO₂ photoreduction. *Nature* **586**, 549–554 (2020).
- Wang, M. T., Wang, D. K. & Li, Z. H. Self-assembly of CPO-27-Mg/TiO₂ nanocomposite with enhanced performance for photocatalytic CO₂ reduction. *Appl. Catal. B* **183**, 47–52 (2016).
- Yan, S. S. et al. Co-ZIF-9/TiO₂ nanostructure for superior CO₂ photoreduction activity. *J. Mater. Chem. A* **4**, 15126–15133 (2016).
- Schukraft, G. E. M. et al. Hypercrosslinked polymers as a photocatalytic platform for visible-light-driven CO₂ photoreduction using H₂O. *ChemSusChem* <https://doi.org/10.1002/cssc.202002824> (2021).
- Zhang, H. B. et al. Efficient visible-light-driven carbon dioxide reduction by a single-atom implanted metal-organic framework. *Angew. Chem. Int. Ed.* **55**, 14310–14314 (2016).
- Cavka, J. H. et al. A new zirconium inorganic building brick forming metal organic frameworks with exceptional stability. *J. Am. Chem. Soc.* **130**, 13850–13851 (2008).
- Sun, D. R. et al. Studies on photocatalytic CO₂ reduction over NH₂-UiO-66 (Zr) and its derivatives: towards a better understanding of photocatalysis on metal-organic frameworks. *Chem. Eur. J.* **19**, 14279–14285 (2013).
- Furukawa, H., Cordova, K. E., O'Keeffe, M. & Yaghi, O. M. The chemistry and applications of metal-organic frameworks. *Science* **341**, 1230444–1230456 (2013).
- Kalmutzki, M. J., Hanikel, N. & Yaghi, O. M. Secondary building units as the turning point in the development of the reticular chemistry of MOFs. *Sci. Adv.* **4**, eaat9180 (2018).
- Trickett, C. A. et al. Definitive molecular level characterization of defects in UiO-66 crystals. *Angew. Chem. Int. Ed.* **54**, 11162–11167 (2015).
- Vos, A. D., Hendrickx, K., Van Der Voort, P., Van Speybroeck, V. & Lejaeghere, K. Missing linkers: an alternative pathway to UiO-66 electronic structure engineering. *Chem. Mater.* **29**, 3006–3019 (2017).
- Deng, W. Y. et al. Crucial role of surface hydroxyls on the activity and stability in electrochemical CO₂ reduction. *J. Am. Chem. Soc.* **141**, 2911–2915 (2019).
- Mu, R. T., Zhao, Z. J., Dohnálek, Z. & Gong, J. L. Structural motifs of water on metal oxide surfaces. *Chem. Soc. Rev.* **46**, 1785–1806 (2017).
- Chevreau, H. et al. Concentration-dependent binding of CO₂ and CD₄ in UiO-66(Zr). *J. Phys. Chem. C* **119**, 6980–6987 (2015).
- Grissom, T. G. et al. Molecular-level insight into CO₂ adsorption on the zirconium based metal-organic framework, UiO-66: a combined spectroscopic and computational approach. *J. Phys. Chem. C* **123**, 13731–13738 (2019).
- Shido, T. & Iwasawa, Y. Regulation of reaction intermediate by reactant in the water-gas shift reaction on CeO₂ in relation to reactant-promoted mechanism. *J. Catal.* **136**, 493–503 (1992).
- Sun, S. et al. Photocatalytic oxidation of gaseous formaldehyde on TiO₂: an in-situ DRIFTS study. *Catal. Lett.* **137**, 239–246 (2010).
- Graciani, J. et al. Highly active copper-ceria and copper-ceria-titania catalysts for methanol synthesis from CO₂. *Science* **345**, 546–550 (2014).
- Gao, S. et al. Partially oxidized atomic cobalt layers for carbon dioxide electroreduction to liquid fuel. *Nature* **529**, 68–71 (2016).
- Shao, X. Z. et al. Iridium single-atom catalyst performing a quasi-homogeneous hydrogenation transformation of CO₂ to formate. *Chem* **5**, 693–705 (2019).
- Kamada, K., Jung, J. & Saito, S. Photocatalytic CO₂ reduction using a robust multifunctional iridium complex toward the selective formation of formic acid. *J. Am. Chem. Soc.* **142**, 10261–10266 (2020).
- Dan-Hardi, M. et al. A new photoactive crystalline highly porous titanium(IV) dicarboxylate. *J. Am. Chem. Soc.* **131**, 10857–10859 (2009).
- Freakley, S. J. et al. Palladium-tin catalysts for the direct synthesis of H₂O₂ with high selectivity. *Science* **351**, 965–968 (2016).
- Liu, Z. Y. et al. High-efficiency oxygen reduction to hydrogen peroxide catalysed by oxidized carbon materials. *Nat. Catal.* **1**, 156–162 (2018).

Acknowledgements

The authors acknowledge the Analytical and Testing Center of BIT for technical supports. A.X.Y. acknowledges the financial support by the National Natural Science Foundation of China (No. 21971012), the Beijing Municipal Natural Science Foundation (JQ20007), and the Beijing Institute of Technology Research Fund Program for Young Scholars. X.F. acknowledges the National Natural Science Foundation of China

(No. 21922502). B.W. acknowledges the National Key Research and Development Program of China (2020YFB1506300), National Natural Science Foundation of China (No. 21971017 and 21625102), and Beijing Institute of Technology Research Fund Program.

Author contributions

A.X.Y. and B.W. designed the research. Y.C.H. and L.W.C. synthesized the catalysts, conducted the structure analysis and photocatalytic studies. Y.C.H., L.W.C., Y.G., Y.W.Z., C.H.Y., M.S., and R.S. performed the X-ray-absorption fine-structure analysis. Q.H.Z. and L.G. performed the electron microscopy study. J.N.L., X.S., W.Y.G., S.W.L., Z.L.Y., and X.F. assisted with the material synthesis, characterizations, and catalysis measurements. Y.C.H. and A.X.Y. co-wrote the paper. A.X.Y. and B.W. supervised the research. All authors discussed the results and assisted during manuscript preparation.

Competing interests

The authors declare no competing interests.

Additional information

Supplementary information The online version contains supplementary material available at <https://doi.org/10.1038/s41467-021-22991-7>.

Correspondence and requests for materials should be addressed to A.-X.Y., R.S. or B.W.

Peer review information *Nature Communications* thanks the anonymous reviewers for their contributions to the peer review of this work. Peer review reports are available.

Reprints and permission information is available at <http://www.nature.com/reprints>

Publisher's note Springer Nature remains neutral with regard to jurisdictional claims in published maps and institutional affiliations.



Open Access This article is licensed under a Creative Commons Attribution 4.0 International License, which permits use, sharing, adaptation, distribution and reproduction in any medium or format, as long as you give appropriate credit to the original author(s) and the source, provide a link to the Creative Commons license, and indicate if changes were made. The images or other third party material in this article are included in the article's Creative Commons license, unless indicated otherwise in a credit line to the material. If material is not included in the article's Creative Commons license and your intended use is not permitted by statutory regulation or exceeds the permitted use, you will need to obtain permission directly from the copyright holder. To view a copy of this license, visit <http://creativecommons.org/licenses/by/4.0/>.

© The Author(s) 2021